05

Analysis of femtosecond modification of thin a-$Ge_2Sb_2Te_5$ films by xz-scan

© I.A. Budagovsky[1], D.O. Kuzovkov[1,2,3], P.I. Lazarenko[2], M.P. Smayev[1]

[1] Lebedev Physical Institute, Russian Academy of Sciences,
119991 Moscow, Russia
[2] National Research University of Electronic Technology,
124498 Zelenograd, Moscow, Russia
[3] „Lasers and instruments“,
124498 Zelenograd, Moscow, Russia

e-mail: BudagovskyIA@mail.ru

Received December 11, 2023
Revised January 09, 2024
Accepted January 16, 2024

Light-induced modification of thin $Ge_2Sb_2Te_5$ chalcogenide films using femtosecond laser radiation in the near-IR range (1030 nm) was studied. By means of two-coordinate (XZ) scanning, a modification stripe was recorded on the surface of the film. When the sample was shifted along the beam axis, the parameters of the acting radiation changed due to a change in the size of the irradiated area, which ensured a consistent change in the characteristic modes of modification: the formation of periodic two-phase surface structures, crystallization, pre-ablation structures, and ablation. The location of modification zones on the recorded stripe correlates with the radiation energy density, which makes XZ-scan a convenient way to determine both the radiation parameters necessary for film modification and the beam geometry.

Keywords: laser modification, femtosecond pulses, thin films, amorphous chalcogenides, optical microscopy.

DOI: 10.61011/EOS.2024.01.58286.7-24

Introduction

Thin-film phase-change chalcogenide-based materials have unique electrical and optical properties that cause research and applied interest in these compounds [1–3]. Vivid example is a triple compound $Ge_2Sb_2Te_5$ — a promising material widely used for data storage, light beam modulation, creation of microphotonics and nanophotonics components, and integral optics [4–6]. As a result of external impact, $Ge_2Sb_2Te_5$ thin films are able to switch quickly (tens of nanoseconds) and reversibly between crystalline and amorphous states that differ considerably in their properties, in particular, conductivity, extinction coefficient, refraction index, etc.

Switching between phase states may be implemented by various methods (thermal, electrical, optical) with laser-beam switching having a special place among them. For crystallization of amorphous surface, heating is required above the crystallization temperature that is about $130-180^\circ$C for $Ge_2Sb_2Te_5$ and may be achieved by means of optical exposure [7–9]. For a reverse process (induced amorphization), heating above the melting temperature and quick cooling (about 10 ns) are required and may be provided at short exposure times, for example, during short laser pulse irradiation [10–12].

When $Ge_2Sb_2Te_5$ is exposed to femtosecond and picosecond light pulses, more complex surface processes may occur resulting, for example, in formation of laser-induced periodic surface structures (LIPSS) in the form of alternating crystalline and amorphous lines [13–16] or in formation of pre-ablation periodic modification [15,17]. LIPSS occurrence is generally associated with formation of a plasmon polariton at the exposed film boundary and plasmon polariton interference with the incident emission [13,14,18]. Multiple studies are devoted to the investigation of laser-beam modification of thin-film structures, where film formation methods, composition, doping components, availability of protective and functional layers, spatial, polarization, energy properties of the affecting emission are varied. With such wide variety of approaches, it becomes important to provide a simple way of characterization of the exposed samples in terms of various physical effects.

As shown in [13,16,19], femtosecond emission parameters (at $\lambda = 1030$ nm) resulting in formation of contrast two-phase LIPSS perpendicular to beam polarization on the surface of $Ge_2Sb_2Te_5$ film are in a quite narrow energy range(maximum energy flux density $F_{\max} = 4-8$ mJ/cm^2), require many pulses (> 250) and are weakly dependent on frequency within $10-1000$ kHz. Such features not only determine the importance of search for the best laser emission parameters for modification, but also allow considering the laser modification of $Ge_2Sb_2Te_5$ chalcogenide film as a kind of indicator of spatial properties of laser emission. Crystalline and amorphous regions of $Ge_2Sb_2Te_5$ differ considerably in refraction and extinction indices resulting in different visible reflection from the film [20] and providing the opportunity to use optical microscopy for modification region analysis.

Generally, to determine emission parameters needed for occurrence of various modification modes, dots array recording experiments are conducted with variable waist, energy, duration, repetition rate and pulse count, which is quite a labor-consuming operation. Herein, we offer a two-axis scanning method where sample movement along the light beam axis ensures the variation of beam size, energy density and pulse count, while the movement in the sample plane allows scanning and recording of these changes in the form of a long modification zone. Such long trace recording demonstrates a full set of possible occurrence of laser modification of $Ge_2Sb_2Te_5$ film: periodic surface structures, continuous crystallization zones, pre-ablation structure and full ablation zones are formed. By comparing the spatial distribution of laser emission with the recorded trace shape and structure, you can determine parameters at which each of the zones typical for femtosecond modification of $Ge_2Sb_2Te_5$ was manifested.

Materials and experimental procedure

As a test sample, 130 nm, amorphous $Ge_2Sb_2Te_5$ film was used. The film was applied to the surface of a 470 μm silicon plate by polycrystalline target magnetron sputtering above the 1 μm SiO_2 layer. The temperature range of transition from amorphous to crystalline state was measured by the temperature dependence of resistivity. It has been found that the phase transition takes place from 160°C to 180°C.

The experimental setup for optical modification of the film (Figure 1) was based on a femtosecond laser system with TETA-20/200-HE-SP feedback amplifier (Avesta, $\lambda = 1030$ nm, minimum pulse duration $\tau = 250$ fs, maximum mean power $P = 20$ W) and hurrySCAN III 14 galvanometric scanner (SCANLAB) with LINOS F-Theta Ronar lens (focal distance 70 mm). Such system forms a beam with waist spot diameter $2w = 27\,\mu$m (by intensity level $1/e^2$). Laser beam geometry and power were defined using BP209-VIS (ThorLabs) profilometer and Nova II (Ophir) meter. Measurement of the beam profile in movement along the optical axis (profilometer movement along the Z axis) was used to determine the offset between the waists in ZX and ZY planes: $\Delta_{exp} = 300-400\,\mu$m.

Irradiation parameters. For $Ge_2Sb_2Te_5$ film irradiation, the mean laser emission power was P=100 mW, pulse duration was τ=250 fs, light beam polarization was parallel to the scanning direction (along the X axis). To record the modification band, the best parameters were selected preliminary (with normal light beam incidence without sample movement along the Z axis) to fit the formation of a maximum wide band in the pre-ablation mode with laser-induced two-phase periodic surface structures with even borders, but without solid crystallization zone. In our case, this was achieved in a diverging beam (2 mm rom the focal plane) and during scanning at a rate of $V_x = 400\,\mu$m/s and pulse repetition rate $\nu = 100$ kHz. The pulse count N_p per

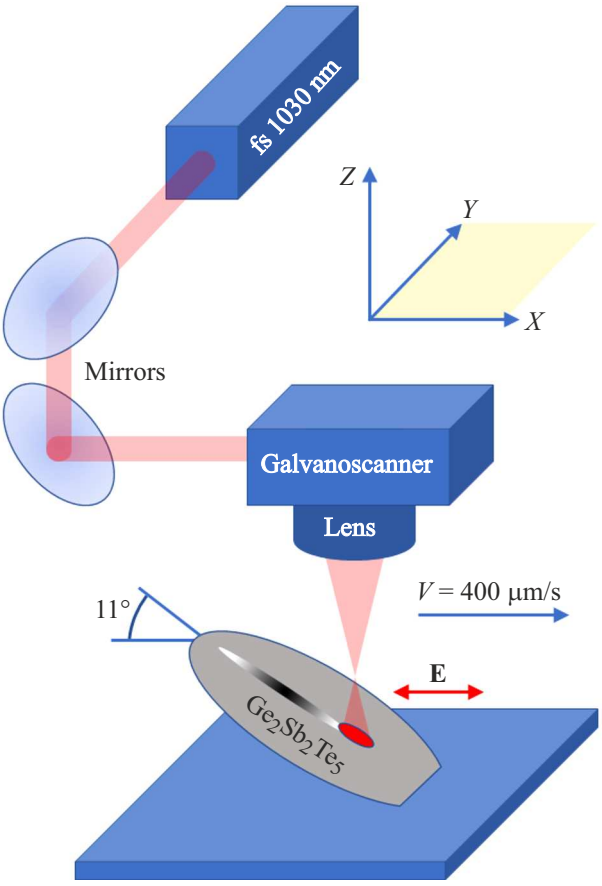

Figure 1. Experimental setup based on the 1030 nm femtosecond laser. Mirrors, Galvanoscanner for beam position control, Lens — a focusing lens, $Ge_2Sb_2Te_5$ — a sample placed at 11° to the horizontal plane. **E** shows the laser emission polarization direction.

surface point defined by

$$N_p = D\frac{\nu}{V_x}, \quad (1)$$

as described in [21] where $D = 2w_x$ is the beam diameter on the sample exceeding 10^3 that agrees well with known data on the pulse count needed for the occurrence of amorphous-crystalline LIPSS [16,19].

Two-axis XZ-scanning was implemented by placement of the sample at an angle to XY plane (Figure 1) and beam movement along the X axis. The sample inclination angle and scanning start point were chosen such as to make the irradiation point move by several millimeters along the Z axis during beam movement, passing the waist position $Z = 0$ (moving from the converging beam to the diverging beam). The corresponding change in the exposed region dimensions ensured the emission parameter variation range, in particular, energy density, that is sufficient for occurrence of various modification modes. The sample inclination angle was equal to 11°, offset in scanning along the X axis was 3 cm.

Analysis of the modified region, its dimensions and shape was conducted using BiOptic SM-300 polarization optical

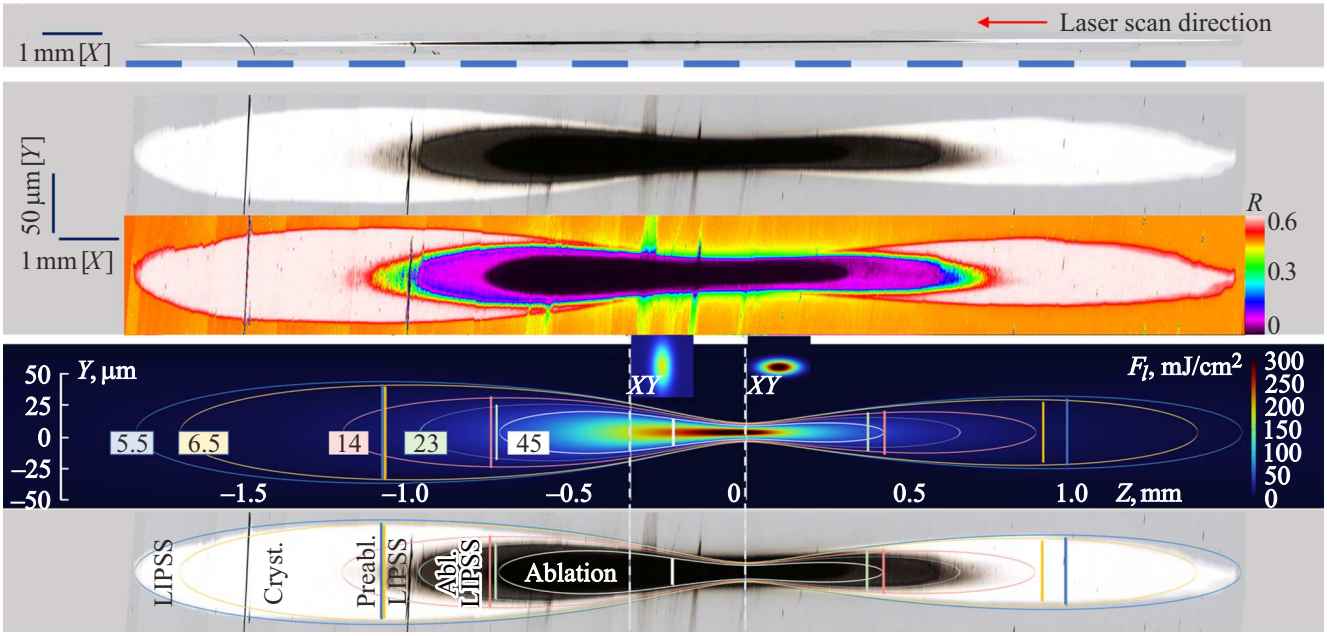

Figure 2. (*a*) Recorded modification band image, (*b*) the same image extended by a factor of 20 along *Y*, and (*c*) corresponding reflectance color chart. (*d*) Numerical simulation of distribution of emission energy density F_l in plane *YZ*. Colored lines show the constant energy density regions (isolines F_l) fitted by experimentally measured modification zone widths (vertical segments). The bars show positions of waists w_{0x} and w_{0y} of the calculated astigmatic beam, corresponding energy density distributions in plane *XY* are given near them. (*e*) Superimposition of energy density isolines on the image Figure 2, *b*.

microscope (Opto-Edu) outfitted with SIMAGIS TC-63CU 12 megapixel CMOS camera. Reflectance

$$R = \frac{(n-1)^2 + k_{\text{ext}}^2}{(n+1)^2 + k_{\text{ext}}^2}, \qquad (2)$$

where n is the refraction index, and k_{ext} is the extinction coefficient that for the visible range is equal to 0.43 (for amorphous film) and 0.61 (for crystallized film). $n^a = 4.2$, $k_{\text{ext}}^a = 0.5$ and $n^c = 6.5$, $k_{\text{ext}}^c = 2$ for the amorphous and crystalline phases of $Ge_2Sb_2Te_5$ were taken from [22]. Considerable difference in reflectances gives an opportunity to highlight modification zones on the image produced using the optical microscope in reflection mode. It can be believed that the reflectance is linearly correlated with crystallinity χ (as described in [23]), therefore, this quantity may be assumed proportional to the image brightness in the regions where the brightness is higher than the background brightness (the background corresponds to the reflection from the non-modified amorphous surface of $Ge_2Sb_2Te_5$ film).

Findings and discussion

XZ-scanning reflects the modification result with various emission parameters (that vary as a result of irradiation point movement along the *Z* axis) to the *X* axis in the form of modification line. The line recorded in such way makes it possible to compare the emission parameters such as beam size, energy density and pulse count per point with the shape of recorded local modification. It should be noted that the change in scanning direction (movement from the diverging beam to the converging beam and vice versa) did not affect the type of recorded modification band and location of typical zones.

In our case, the recorded line length (Figure 2, *a*) was 19.2 mm (this corresponds to the movement along *Z* from −2 to 1.6 mm). The extended (along *Y*) image of the recorded band (Figure 2, *b*) shows several typical zones that differ in reflectance and structure. Considerable differences in reflectance are well illustrated by the color chart (Figure 2, *c*), where the image brightness was represented in the form of a color sequence. This image was used to identify the zone boundaries, for each of which the width vs. the longitudinal position *X* was measured (Figure 3). A total of eight zones qualitatively different in the image structure were observed. A periodic surface structure zone consisting of amorphous and crystalline phase lines (zone *1*) was the most outlying and had a constant crystallization band (zone *2*) in the center. With increasing power density this region became fully crystallized (zone *3*). Then, amorphous and crystalline lines occurred again and could be associated with periodic re-amorphization or with LIPSS reformation above the re-amorphized region (zone *4*). In zones *5, 6* and *7*, pre-ablation processes occurred as described in detail in [17]: formation of Ge $_2$ Sb $_2$ Te $_5$ nanospheres (zone *5*), formation of ridges and dips due to mass transfer (zone *6*) and formation of periodic structures (zone *7*). The last

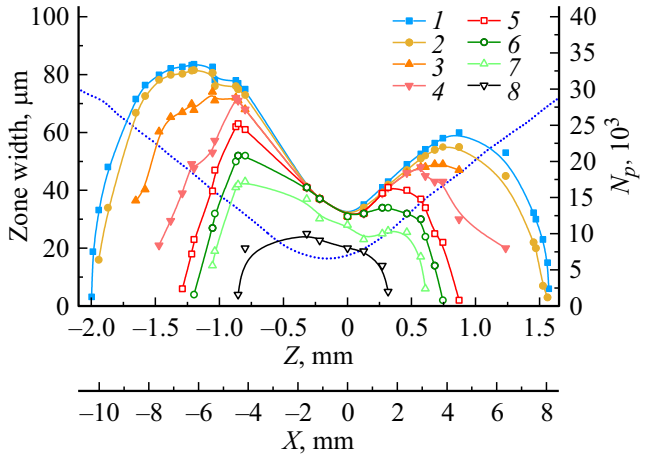

Figure 3. Experimental dependences of various modification zone sizes in the recorded line on position: *1* — two-phase amorphous-crystalline LIPSS zone; *2* — partial crystallization zone; *3* — maximum crystallization zone; *4* — repeated two-phase LIPSS zone; *5* — pre-ablation equidistant nanosphere formation zone; *6* — zone of periodic structure formation due to mass transfer; *7* — ablation LIPSS zone; *8* — ablation zone. Dotted line corresponds to the number of femtosecond pulses N_p falling on the surface point. The X axes show the beam movement relative to the sample vertically (Z) and horizontally (X).

zone (*8*) corresponded to full failure of $Ge_2Sb_2Te_5$ film due to ablation processes.

As shown in Figure 2, *b* and Figure 3, the recorded band has pronounced asymmetry in the longitudinal direction corresponding to scanning on X (and on Z, because the sample is placed at an angle to the XY plane). The shapes of modification regions are different in the diverging and converging beams: maximum width of the recorded region in the diverging beam achieved 84 μm, and in the converging beam — achieved60 μm. Such difference is caused by beam astigmatism and, therefore, by beam ellipticity. Considering this fact, we assessed the local energy density of the affecting emission using the Gaussian distribution with different waists and focal plane positions for orthogonal components:

$$F_l(x,y,z) = \frac{1}{\nu}\frac{2P}{\pi w_{0x} w_{0y}}\frac{w_{0x}}{w_x}\frac{w_{0y}}{w_y} e^{-\frac{2x^2}{w_{0x}^2}} e^{-\frac{2y^2}{w_{0y}^2}}, \qquad (3)$$

where w_{0x}, w_{0y} are waist radii,

$$w_x(z) = w_{0x}\sqrt{1+\frac{z^2}{Z_{rx}^2}}, \qquad (4)$$

$$w_y(z) = w_{0y}\sqrt{1+\frac{(z+\Delta)^2}{Z_{ry}^2}}, \qquad (5)$$

$$Z_{rx} = \frac{\pi w_{0x}^2}{\lambda}, \quad Z_{ry} = \frac{\pi w_{0y}^2}{\lambda}, \qquad (6)$$

Δ — distance between waists, Z_{rx} and Z_{ry} — Rayleigh lengths along the corresponding axes. Calculation of F_l used $w_{0x} = 6\,\mu$m and $w_{0y} = 8.5\,\mu$m corresponding to the Gaussian mode parameters and matching well with experimental energy density distribution at $|Z| > Z_{rx}, Z_{ry}$, but considerably different from the measured w_{0x} and w_{0y} near the waist. $\Delta = 350\,\mu$m used for the calculations is within the experimentally measured Δ_{exp}. Location and width of each of the modification zones within $|Z| > Z_{rx}, Z_{ry}$ match well with the lines with equal energy density (Figure 2, *d*), which is demonstrated by superimposition of isolines onto the zone boundaries (Figure 2, *e*). Near the focal region ($|Z| < Z_{rx}, Z_{ry}$) , the recorded zone width (30 μm) is much larger than the calculated beam size, but matches the experimentally measured value (27 μm). It should be noted that energy density isolines calculated using (3) may be superimposed only at particular w_{0x}, w_{0y} and Δ, therefore the modified region image may be used to define the properties of the affecting light beam with unknown geometry.

With distance from the focus position the exposed region size increases and, in accordance with relation (1), the pulse count N_p per sample surface point increases (Figure 3, dotted line). In our case, N_p varied several times (from $6.5\cdot10^3$ to $33\cdot10^3$), however, the zone boundaries matched exactly with the energy density. Thus, the pulse count in the given range has a low influence on the modification process and the energy density is the determining factor that corresponds to the results of [16,19]. As shown in Figure 3, curves *1* and *2* are close to each other throughout the modification line length suggesting an extremely narrow energy range of amorphous-crystalline structure occurrence.

Consider in greater detail appearance of various effects in the highlighted modification zones (Figure 4). With movement towards the focus and corresponding increase in the energy density, periodic objects around defects on the film surface occur first (Figure 4, *c*), that matches with the decrease in energy threshold of LIPSS formation observed in [24]. Then, continuous zone of regular periodic structures is formed from crystalline and amorphous phase lines oriented perpendicularly to the light field polarization and alternating in a period close to the wavelength (Figure 4, *d, e, n, o*). Such surface modification represents low spatial frequency-laser induced periodic surface structures (LSF-LIPSS) [18], whose occurrence is generally associated with formation of a surface plasmon polariton and further interference with incident emission [14,16,18]. Local energy density F_l in the regions of starting amorphous-crystalline LIPSS formation was about 5 mJ/cm^2. Continuous zone of regular LIPSS corresponded to $F_l > 5.5$ mJ/cm^2 (Figure 4, *d, e, o*) and also was observed throughout the external boundary of the modified region (periphery Figure 4, *f–n*). Whole amorphous-crystalline LIPSS zone falls within $F_l = 5.5{-}6.5$ mJ/cm^2, which matches well with the results of [13,16] (these studies report the mean energy densities that are about two times lower than the local values of F_l).

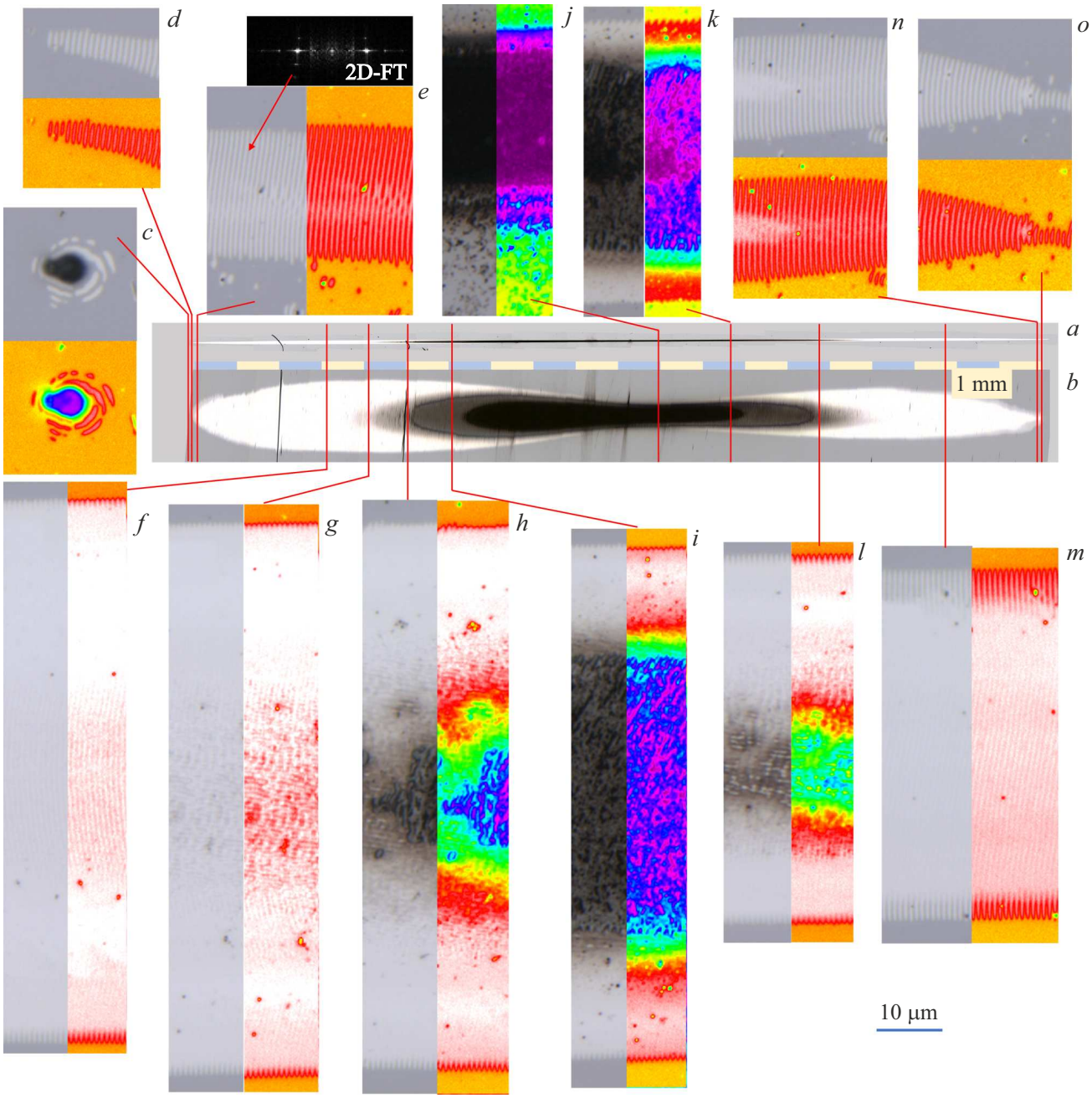

Figure 4. (*a*) Image of the recorded band obtained using the optical microscope and (*b*) extended by a factor of 20 vertically. (*c*–*o*) Magnified images and color charts of brightness for the modification areas shown by red lines and corresponding to various laser exposure conditions: (*c*) amorphous-crystalline LIPSS near defects; (*d*, *o*) beginning and end of the modification band; (*e*) regular amorphous-crystalline LIPSS and corresponding Fourier transform; (*f*, *m*) full crystallization regions against the LIPSS background; (*g*, *l*) occurrence of nanospheres against the crystallized zone background (maximum modification band width); (*h*, *i*) ablation LIPSS at the pre-ablation region boundary; (*j*) ablation region (minimum band width); (*k*) ablation LIPSS and ablation start in the central area; (*l*) occurrence of pre-ablation periodic structures due to mass transfer; (*n*) occurrence of partial crystallization against the LIPSS background. Image scale (*c*–*o*) is shown in the lower right-hand corner.

Beginning from $F_l > 6.5\,\text{mJ/cm}^2$, LIPSS contrast starts decreasing in the band center (Figure 4, *m*) suggesting that a solid crystallized region starts forming. With further increase in the energy density up to $14\,\text{mJ/cm}^2$ together with the increase in the full crystallization zone width in the center, periodic structures occur again (Figure 4, *e*), which may be due to reformation of LIPSS on the region re-amorphized by a femtosecond beam or due to periodic re-amorphization.

Further increase in F_l results in occurrence of particular pre-ablation and ablation effects (Figure 4, *g*–*l*). Here, we

shall note a zone (Figure 4, *g, l*) with $F_l = 15-20\,\mathrm{mJ/cm^2}$ where equidistant nanospheres of amorphous $Ge_2Sb_2Te_5$ are formed. With increasing energy density ($F_l = 20-45\,\mathrm{mJ/cm^2}$), they become an ablation periodic structure (Figure 4, *h, i, l*) (these processes are described in detail in [17]). Finally, in the maximum energy density region near the beam waist, almost whole modification region corresponds to material ablation from the substrate surface (Figure 4, *j, k*).

Thus, the position of all typical zones recorded in scanning matches well the energy density isolines. Since many of the effects considered for $Ge_2Sb_2Te_5$ film appear during the change in the lase emission energy density in many other materials, then the offered two-axis scanning method will be relevant for them.

Conclusion

The investigations of femtosecond modification of a thin amorphous film have shown that the offered method od simultaneous scanning along *X* and *Z* makes it possible to form in one pass and then to analyze the main laser exposure effects on the phase-change material surface: formation of two-phase periodic structures, crystallization, formation of pre-ablation periodic structures and ablation film failure. XZ-scanning makes it possible to determine energy boundaries of typical processes observed in laser exposure. Thus, for $Ge_2Sb_2Te_5$, the energy density range for formation of two-phase LIPSS is $F_l = 5-7\,\mathrm{mJ/cm^2}$, the uniform crystallization range is $F_l = 7-15\,\mathrm{mJ/cm^2}$, pre-ablation periodic structures form at $F_l = 15-45\,\mathrm{mJ/cm^2}$, and ablation occurs at a higher value.

Beam shape distortion (astigmatism, ellipticity, etc.) does not limit the method applicability. On the contrary, if it is difficult to identify the beam parameters (for example, due to high pulse energy or specific wavelength), then the arrangement and shape of typical modification zones make it possible to assess the distribution of the acting emission energy density in longitudinal and transverse directions. This feature seems promising for materials showing various light-induced phenomena, and the case of structures forming in a narrow energy range such as pre-ablation LIPSS is of particular interest. Such materials include phase-change materials, in particular, $Ge_2Sb_2Te_5$ film of interest. The effect of ultra-short pulses (femtosecond and picosecond) makes it possible to implement the highest amount of $Ge_2Sb_2Te_5$ surface modification effects, however, the offered approach is also applicable to longer optical pulses (up to continuous emission).

Funding

The study was supported by grant No 23-29-00977 provided by the Russian Science Foundation https://rscf.ru/project/23-29-00977/.

Conflict of interest

The authors declare that they have no conflict of interest.

References

[1] J. Hegedüs, S.R. Elliott. Nat. Mater., **7** (5), 399 (2008). DOI: 10.1038/nmat2157
[2] M. Wuttig, N. Yamada. Nat. Mater., **6** (11), 824 (2007). DOI: 10.1038/nmat2009
[3] S. Abdollahramezani, O. Hemmatyar, H. Taghinejad, A. Krasnok, Y. Kiarashinejad, M. Zandehshahvar, A. Alú, A. Adibi. Nanophotonics, **9** (5), 1189 (2020). DOI: 10.1515/nanoph-2020-0039
[4] Q. Wang, E.T.F. Rogers, B. Gholipour, C.-M. Wang, G. Yuan, J. Teng, N.I. Zheludev. Nat. Photonics, **10** (1), 60 (2016). DOI: 10.1038/nphoton.2015.247
[5] Z. Guo, X. Yang, F. Shen, Q. Zhou, J. Gao, K. Guo. Sci. Rep., **8** (1), 12433 (2018). DOI: 10.1038/s41598-018-30550-2
[6] S.A. Kozyukhin, P.I. Lazarenko, A.I. Popov, I.L. Eremenko. Russ. Chem. Rev., **91** (9), RCR5033 (2022). DOI: 10.1070/RCR5033.
[7] I. Friedrich, V. Weidenhof, S. Lenk, M. Wuttig. Thin Solid Films, **389** (1), 239 (2001). DOI: 10.1016/S0040-6090(01)00891-4
[8] J. Fu, X. Shen, Y. Xu, G. Wang, Q. Nie, C. Lin, S. Dai, T. Xu, R. Wang. Mater. Lett., **88**, 148 (2012). DOI: 10.1016/j.matlet.2012.08.051
[9] G. D'Arrigo, M. Scuderi, A. Mio, G. Favar., M. Conte, A. Sciuto, M. Buscema, G. Li-Destri, E. Carria, D. Mello, M. Calabretta, A. Sitta, J. Pries, E. Rimini. Mater. Design, **202**, 109545 (2021). DOI: 10.1016/j.matdes.2021.109545
[10] Y. Liu, M.M. Aziz, A. Shalini, C.D. Wright, R.J. Hicken. J. Appl. Phys., **112** (12) (2012). DOI: 10.1063/1.4770359
[11] A.V. Kiselev, V.V. Ionin, A.A. Burtsev, N.N. Eliseev, V.A. Mikhalevsky, N.A. Arkharova, D.N. Khmelenin, A.A. Lotin. Opt. Laser Technol., **147**, 107701 (2022). DOI: 10.1016/j.optlastec.2021.107701
[12] S.A. Kozyukhin, P.I. Lazarenko, Yu.V. Vorobyov, M.S. Savelyev, A.A. Polokhin, V.B. Glukhenkaya, A.A. Sherchenkov, A.Y. Gerasimenko. Mater. Tech., **107** (3), 307 (2019). DOI: 10.1051/mattech/2019008
[13] S. Kozyukhin, M. Smayev, V. Sigaev, Yu. Vorobyov, Yu. Zaytseva, A. Sherchenkov, P. Lazarenko. Phys. Status Solidi B, **257** (11), 1900617 (2020). DOI: 10.1002/pssb.201900617
[14] S. Zabotnov, A. Kolchin, D. Shuleiko, D. Presnov, T. Kaminskaya, P. Lazarenko, V. Glukhenkaya, T. Kunkel, S. Kozyukhin, P. Kashkarov. Micro, **2** (1), 88 (2022). DOI: 10.3390/micro2010005
[15] K. Zhao, W. Han, Z. Han, X. Zhang, X. Zhang, X. Duan, M. Wang, Y. Yuan, P. Zuo. Nanophotonics, **11** (13), 3101 (2022). DOI: 10.1515/nanoph-2022-0133
[16] M.P. Smayev, P.I. Lazarenko, I.A. Budagovsky, A.O. Yakubov, V.N. Borisov, Yu.V. Vorobyov, T.S. Kunkel, S.A. Kozyukhin. Opt. Laser Technol., **153**, 108212 (2022). DOI: 10.1016/j.optlastec.2022.108212
[17] T. Kunkel, Yu. Vorobyov, M. Smayev, P. Lazarenko, A. Kolobov, S. Kozyukhin. Appl. Surf. Sci., **624**, 157122 (2023). DOI: 10.1016/j.apsusc.2023.157122
[18] J. Bonse, A. Rosenfeld, J. Krüger. J. Appl. Phys., **106** (10) (2009). DOI: 10.1063/1.3261734

[19] M.P. Smayev, P.I. Lazarenko, M.E. Fedyanina, I.A. Budagovsky, A. Raab, I.V. Sagunova, S.A. Kozyukhin. Opt. Spectrosc., **131** (2), 185 (2023). DOI: 10.61011/EOS.2023.02.55783.15-23.
[20] C. Ruiz de Galarreta, S.G.C. Carrillo, Y.Y. Au, E. Gemo, L. Trimby, J. Shields, E. Humphreys, J. Faneca, L. Cai, A. Baldycheva, J. Bertolotti, C.D. Wright. J. Opt., **22** (11), 114001 (2020). DOI: 10.1088/2040-8986/abbb5b
[21] F. Chen, J.R.V. de Aldana. Las. Photonics Rev., **8** (2), 251 (2014). DOI: 10.1002/lpor.201300025
[22] Ya.S. Lebedeva, M.P. Smayev, I.A. Budagovsky, M.E. Fedyanina, I.S. Sinev, T.S. Kunkel, A.V. Romashkin, P.A. Smirnov, A.A. Sherchenkov, S.A. Kozyukhin, P.I. Lazarenko. J. Surf. Invest., **17** (Suppl. 1), S339 (2023). DOI: 10.1134/S1027451023070297
[23] V. Weidenhof, I. Friedrich, S. Ziegler, M. Wuttig. J. Appl. Phys., **89** (6), 3168 (2001). DOI: 10.1063/1.1351868
[24] H. Shimizu, S. Yada, G. Obara, M. Terakawa. Opt. Express, **22** (15), 17990 (2014). DOI: 10.1364/OE.22.017990

Translated by E.Ilinskaya